Mineralium Deposita (2020) 55:1353–1364
https://doi.org/10.1007/s00126-019-00940-1

ARTICLE

Mercury and in situ sulfur isotopes as constraints on the metal and sulfur sources for the world's largest Sb deposit at Xikuangshan, southern China

Shanling Fu[1,2] · Ruizhong Hu[1,3] · Runsheng Yin[1] · Jun Yan[1] · Xifeng Mi[1] · Zhengcheng Song[4] · Neal A. Sullivan[2]

Received: 29 July 2019 / Accepted: 18 November 2019 / Published online: 19 December 2019

Abstract

It has been well established that metal and sulfur sources in mineral deposits can be very difficult to identify, especially for ore deposits hosted in sedimentary rocks. Using the world's largest Sb deposit at Xikuangshan in southern China as a case study, this study combined Hg isotopes and in situ sulfur isotope measurements to constrain the sources of Sb and sulfur. A variation of 1.1‰ in δ^{202}Hg (0.04 to 1.15‰) was observed in stibnite ore samples, suggesting that mass-dependent fractionation of Hg isotopes occurred during the formation of the deposit. Significant mass-independent fractionation of Hg isotopes, with Δ^{199}Hg ranging from − 0.03 to − 0.17‰, was also observed in the ore samples, suggesting that Hg transported by the ore fluids was inherited from Proterozoic basement metamorphic rocks as these rocks show similar Δ^{199}Hg signatures (− 0.03 to 0.07‰). In situ sulfur isotope measurements yielded δ^{34}S values that cluster in the range of + 6.8 to + 10.2‰, providing evidence that sulfur contained in ore fluids may also have been dominantly derived from underlying Proterozoic basement metamorphic rocks (δ^{34}S = +5.6 to + 11.5‰). Using the new results from Hg and S isotopes, we proposed that deep-circulated meteoric water mobilized Sb, Hg, and S from the Proterozoic metamorphic basement, ascended along deep faults, and subsequently deposited Sb at favorable structural zones as a result of boiling of the hydrothermal fluids, generating the world-class Xikuangshan Sb deposit. This study also highlights the combined use of Hg-S isotopes as a novel method to provide new and additional insights into the source regions of ore materials for sedimentary-hosted Sb deposits.

Keywords Hg isotopes · In situ sulfur isotopes · Source of ore metals · Xikuangshan Sb deposit

Introduction

Identifying the source region of metals contained in hydrothermal ore deposits hosted in sedimentary rocks is a challenge as conventional isotope signatures may not necessarily constrain metal sourcing. Over the past decade, several studies used unconventional isotopes of ore metals (e.g., Hg, Cu, Fe, Zn, Mo, Pb, Cd, Ge, Re, and Os) as a direct tracer of metal sources (Mathur et al. 2002, 2010; Dauphas et al. 2004; Morelli et al. 2007; Smith et al. 2008; Kelley et al. 2009; Darling et al. 2012; Meng et al. 2015; Yin et al. 2016; Zhu et al. 2017; Debret et al. 2018). However, the application of metal isotopes to hydrothermal ore deposits hosted in sedimentary rocks remains scarce, and therefore, case studies are needed to validate metal isotopes as a viable method for constraining the sources of metals.

Mercury is abundant in sulfide minerals in hydrothermal deposits (Schwartz 1997; Rytuba 2003; Yin et al. 2016). Mercury isotope geochemistry has recently been employed as a tool for understanding the sources of Hg and perhaps other chalcophile metals in hydrothermal ore deposits. Mercury isotopes undergo mass-dependent fractionation (MDF). Since Hg has seven natural stable isotopes (^{196}Hg, ^{198}Hg, ^{199}Hg, ^{200}Hg,

Editorial handling: T. Monecke

✉ Ruizhong Hu
huruizhong@vip.gyig.ac.cn

[1] State Key Laboratory of Ore Deposit Geochemistry, Institute of Geochemistry, Chinese Academy of Sciences, Guiyang 550081, China

[2] Department of Earth Sciences, University of Toronto, Toronto M5S 3B1, Canada

[3] College of Earth and Planetary Sciences, University of Chinese Academy of Sciences, Beijing 100049, China

[4] State Key Laboratory of Environmental Geochemistry, Institute of Geochemistry, Chinese Academy of Sciences, Guiyang 550081, China

^{201}Hg, ^{202}Hg, and ^{196}Hg), with a relative mass difference of 4%, Hg-MDF is readily occurring during most chemical (e.g., photoreduction, ligand exchange, sorption, precipitation, and abiotic methylation), physical (e.g., diffusion, evaporation, and volatilization), and biological processes (e.g., microbial methylation, demethylation) (Bergquist and Blum 2009; Yin et al. 2010). In some cases, the isotope fractionation of Hg is mass-independent, resulting in so-called mass-independent fractionation (MIF). Unlike Hg-MDF, Hg-MIF mainly occurs during photochemical reactions (Blum et al. 2014). A large variation of Hg-MDF and Hg-MIF signals, in terms of δ^{202}Hg and $^{\Delta}{}^{199}$Hg, respectively, have been reported in natural samples. The MIF signature of Hg observed in natural samples is thought to be related to Hg photochemical reactions (Blum et al. 2014; Yin et al. 2016). In hydrothermal processes, the release of Hg from source rocks seems to cause little Hg-MDF ($< \pm 0.5‰$ in δ^{202}Hg; Smith et al. 2008), but the boiling of hydrothermal fluids and redox reactions can result in significant Hg-MDF (up to 4‰ in δ^{202}Hg; Smith et al. 2005). Hydrothermal processes do not cause significant Hg-MIF (Smith et al. 2005, 2008; Sherman et al. 2009; Tang et al. 2017; Yin et al. 2019). The effects of Hg-MIF can therefore act as a direct source tracer of Hg in hydrothermal deposits since syngenetic Hg in magmatic/mantle materials is characterized by the absence of MIF (Δ^{199}Hg ~ 0), but epigenetic Hg in sedimentary rocks show a large variation of Δ^{199}Hg (Yin et al. 2016 and references therein). Some hydrothermal sulfide deposits show small but significant Hg-MIF signals, which have been interpreted by inheritance of epigenetic Hg via sedimentation and hydrothermal leaching (Sonke et al. 2010; Yin et al. 2016; Xu et al. 2018).

In addition, sulfur isotopes can provide a direct constraint on the sources of sulfur in hydrothermal deposits. Although bulk analysis methods for sulfur isotopes can produce high-precision analyses, recent studies have shown that laser ablation multi-collector inductively coupled plasma mass spectrometry (LA-MC-ICP-MS) analyses of sulfur isotopes offer several advantages over bulk analysis method such as higher spatial resolution across individual mineral grains (10–100 μm) and provide useful geochemical information such as features of mineral growth at the sub-grain scale (Craddock et al. 2008; Bühn et al. 2012; Yuan et al. 2018). Therefore, in situ sulfur analysis has been employed as a tool to understand the sources of sulfur in hydrothermal fluids (Mason et al. 2006; Hou et al. 2016).

The Xikuangshan Sb deposit in southern China is the world's largest source of Sb. This deposit has a total proven Sb metal reserve of about 2.5 Mt, with an average grade of about 4% Sb (Hu et al. 2017). Although the deposit has been the focus of several previous studies, the genesis of the ore deposit remains controversial owing to a lack of conclusive constraints on the sources of metals and sulfur. Two opposing viewpoints have been proposed to explain the ore genesis of this deposit: (i) intrusion-related and (ii) strata-bound models (Hu et al. 2017 and references therein). The former argued that ore materials were mainly derived from deep-seated magmas without significant contribution of Devonian host rocks (Liu et al. 1985), whereas the latter proposed that metals in this deposit were dominantly derived from sedimentary and metamorphic rocks without any genetic links to magmas (Chen et al. 1983; Ma et al. 2003).

In this study, we report Hg isotope data from Xikuangshan in conjunction with in situ sulfur isotope data to provide new insights into the sources of Sb, Hg, and S. The study highlights the potential of combined Hg-S isotope measurements to constrain the sources of ore materials for sedimentary-hosted Sb deposits.

Regional and ore deposit geology

The South China Block is made up of the Yangtze Block to the northwest and the Cathaysia Block to the southeast which were welded together along the Jiangshao suture zone (Zhao et al. 2011; Hu and Zhou 2012; Yao et al. 2016; Fig. 1). The Xikuangshan Sb deposit is located in central Hunan province, in the eastern part of the Yangtze Block. Outcropping strata in central Hunan can be defined by two major lithotectonic units: (i) basement low-grade (greenschist facies) metasedimentary rocks of Middle to Late Proterozoic and Early Paleozoic age, and (ii) overlying sedimentary rocks of Late Paleozoic to Cretaceous age (BGMRHN 1988). The former is composed lithologically of thin-layer metasandstones, tuffaceous slates, and megafossiliferous metasedimentary rocks, which are mainly distributed along the margins of the Xiangzhong Basin and some interior sub-uplifts. The latter consists of mainly thick-bedded, massive carbonates,with minor amounts of shales, siltstones, and iron formations (Fig. 1; Liu et al. 1985; Shi et al. 1993; Ma et al. 2002). Early Devonian (410–400 Ma) and Late Triassic (230–200 Ma) graitic rocks outcrop in the periphery of the district (Fu et al. 2015; Chen et al. 2016; Xie et al. 2019).

The Xikuangshan Sb deposit (111° 27′ 30″ E, 27° 40′ 30″ N) is located at the intersection of the NE-striking Chengbu-Taojiang regional fault and NW-striking Xikuangshan-Lianyuan basement fault (Fig. 1). Middle-Upper Devonian and Lower Carboniferous strata are the only rocks exposed in the deposit area, which are dominated by carbonates and locally interbedded with siltstone, argillite, and shale (Peng et al. 2003; Fan et al. 2004). The Sb mineralization is mainly hosted in the central portion of the Devonian Shetianqiao Formation and, to a lesser extent, in the lower part of the Devonian Shetianqiao Formation. The central part of the Devonian Shetianqiao Formation is composed of sandstone, carbonate, and mudstone layers from lower to upper and has a total thickness of > 350 m. The carbonate layer hosts the bulk

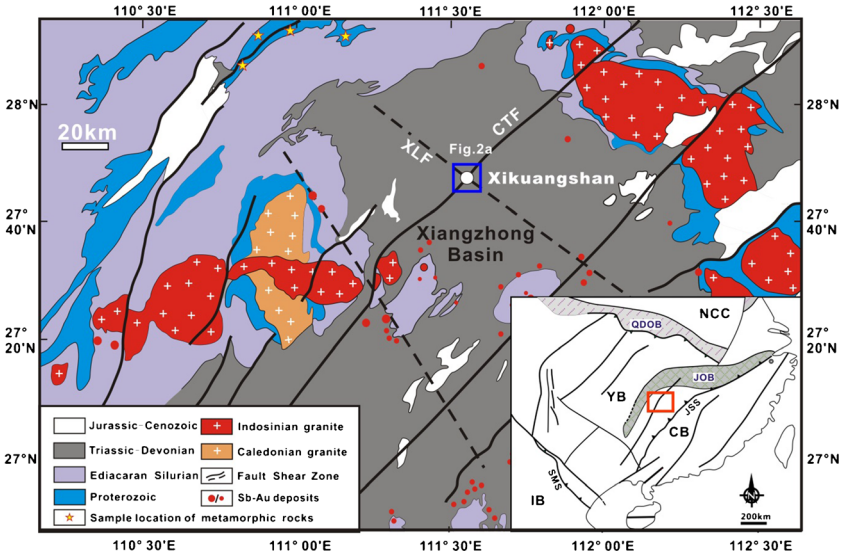

Fig. 1 Location of the Xikuangshan Sb deposit in southern China (modified from Hu et al. 2017). CB Cathaysia Block, IB Indochina Block, JOB Jiangnan Orogen Belt, JSS Jiang-Shao Suture, NCC North China Craton, QDOB Qinling-Dabie Orogen Belt, SMS Song-MA Suture, YB Yangtze Block, XLF Xikuangshan-Lianyuan Fault, CTF Chengbu-Taojiang Fault

of mineralization and is dominantly limestone interlayered with thin sandy mudstone. The mudstone layers above the carbonate layer are thought to have acted as a barrier to rising ore fluids, resulting in the precipitation and accumulation of Sb in the limestone (Jin et al. 2001; Yang et al. 2006a). These strata have been intensely deformed into a kilometer-scale, NNE-trending major fold structure referred as the Xikuangshan complex anticline (Fig. 2a; Peng et al. 2003; Yang et al. 2006b). The fault F_{75}, which is a part of the regional Chengbu-Taojiang fault, cuts the northwest limb of the Xikuangshan complex anticline. Almost all orebodies occur in the footwall of this fault (Fig. 2a). A NNE-trending lamprophyre dike is the only outcropping intrusive rock in the deposit area (Hu et al. 1996; Peng et al. 2003; Fan et al. 2004). Although the precise age remains unclear, the dike is believed to have formed prior to the Sb mineralization (Liu and Jian 1983; Liu et al. 1985; Xie et al. 2001).

The Sb mineralization in the Xikuangshan deposit consists of the four ore blocks, referred to as Laokuangshan, Tongjiayuan, Wuhua, and Feishuiyan (Hu et al. 1996; Peng et al. 2003; Fig. 2a). Orebodies in the Xikuangshan deposit are chiefly stratiform, generally extending from 30 to 600 m along the strike and 1300–1800 m down in dip with a thickness of 1–5 m (locally up to 20 m), and are strictly controlled by interlayer fault zones in silicified carbonates (Fig. 2b). More than 80% of the Sb metal reserves come from stratiform orebodies with irregular hydrothermal veins (Fig. 3). The ores are monotonous in composition with stibnite as the only economic metallic mineral, and no mercury minerals were found; gangue minerals are dominated by quartz and calcite with minor barite, fluorite, talc, and gypsum (Peng et al. 2003; Hu and Peng 2018). The detailed mineral paragenesis for the Xikuangshan deposit is divided into early-stage and late-stage mineralization, and the features of each stage have been documented by Lin (2014) and Hu and Peng (2018). Wall rock alteration related to Sb mineralization comprises dominantly silicification and carbonatization, as well as local weak fluorite alteration (Kuang 2000; Peng et al. 2003). Silicification is pervasive in the deposit and Sb orebodies never appear to exceed the limit of silicic alteration (Fig. 2b; Hu et al. 1996; Yang et al. 2006b). Available fluid inclusion data suggest that the ore-forming fluids at Xikuangshan had epithermal temperatures of 150 to 250 °C and salinities < 5 wt% NaCl equiv. (Lin 2014; Hu and Peng 2018). The data from hydrothermal calcite Sm-Nd dating and (U-Th)/He dating of zircon in altered wall rocks showed that the mineralization is Mesozoic with an age of ca. 120–150 Ma (Peng et al. 2003; Fu et al. 2019).

Samples and analytical methods

Fifteen stibnite ore samples were collected from underground workings at different mine levels ranging from level 25# at an elevation of − 142 m to level 2# at an elevation of + 320 m in the Feishuiyan and Laokuangshan blocks. Three major types of ores were collected (Fig. 4), namely (i) quartz-stibnite; (ii) calcite-quartz-stibnite; and (iii) calcite-stibnite. In addition, seven wall rock samples, including four barren rocks (XKS-2@1, XKS-3@1, XKS-4@2, and XKS-7@2) and three altered rocks (XKS-2@2, XKS-7@6, and XKS-9@2), were collected. As no metamorphic basement rocks were exposed in the Xikuangshan district, four metamorphic rocks were collected from the nearby Xuefengshan uplift (Fig. 1), which is dominated by the metamorphic slate of the Banxi Group.

Mercury isotope analysis

Approximately 100 g of each ore sample was crushed. Stibnite grains were handpicked under a binocular microscope, and

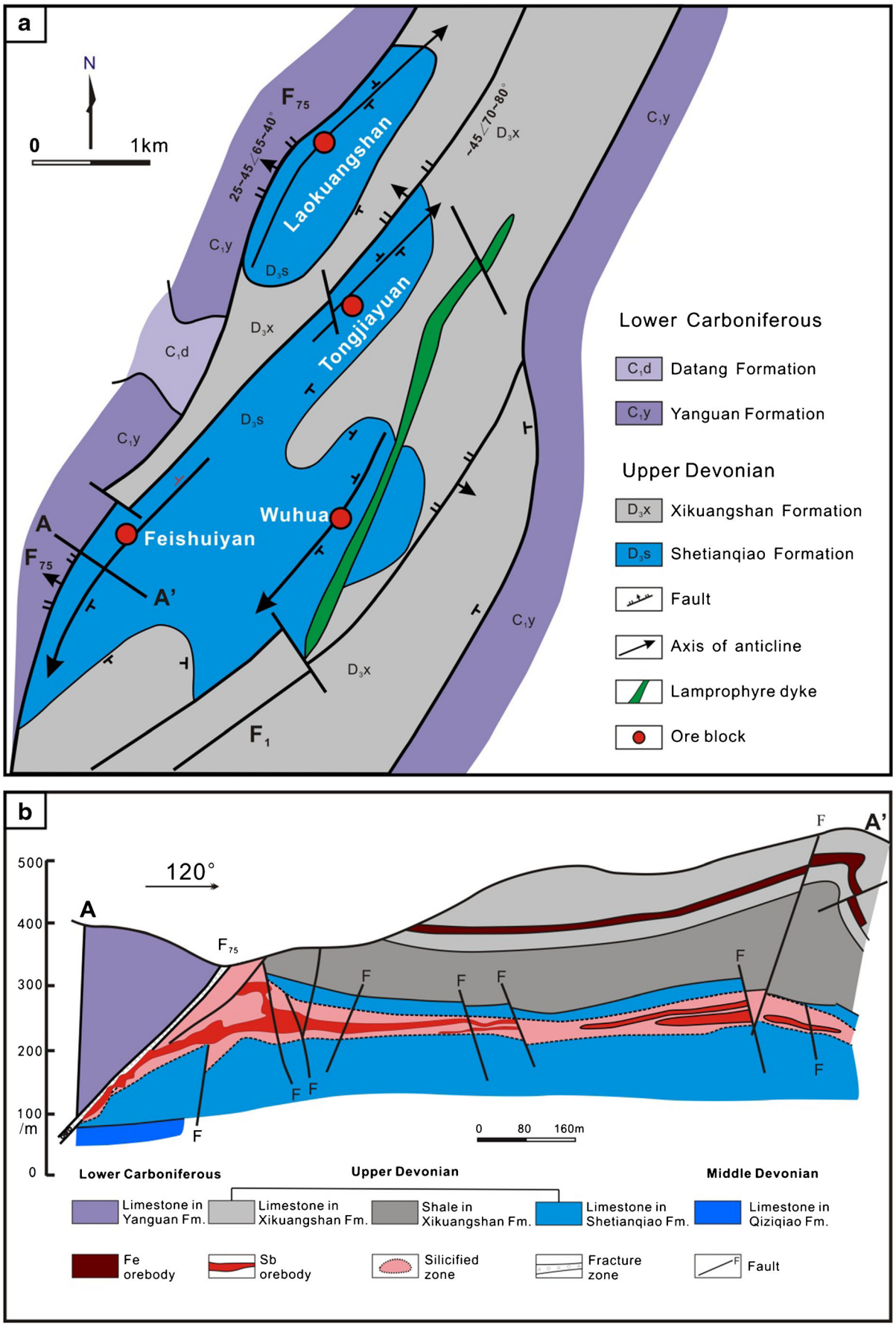
a
N
0
1km
F75
25–45∠65–40°
Laokuangshan
Tongjiayuan
Wuhua
Feishuiyan
A
A'
F1
-45∠70–80°
C1y
C1d
D3s
D3x
Lower Carboniferous
C1d Datang Formation
C1y Yanguan Formation
Upper Devonian
D3x Xikuangshan Formation
D3s Shetianqiao Formation
Fault
Axis of anticline
Lamprophyre dyke
Ore block
b
120°
A
A'
F75
F
500
400
300
200
100
/m
0
0 80 160m
Lower Carboniferous
Upper Devonian
Middle Devonian
Limestone in Yanguan Fm.
Limestone in Xikuangshan Fm.
Shale in Xikuangshan Fm.
Limestone in Shetianqiao Fm.
Limestone in Qiziqiao Fm.
Fe orebody
Sb orebody
Silicified zone
Fracture zone
Fault

◀ **Fig. 2** Geological setting of the Xikuangshan Sb deposit in southern China. **a** Geological map showing the locations of the four ore blocks Laokuangshan, Tongjiayuan, Feishuiyan, and Wuhua (modified after from Peng et al. 2003). **b** A-A' section showing the occurrence of orebodies and their relationship with silicic alteration (modified after Tao et al. 2002)

handpicked stibnites in each sample were combined as a sample, which was manually crushed into 150 mesh in an agate mortar prior to chemical analysis. About 1 kg of each rock sample was crushed and sieved to 150 mesh. Approximately 0.1 g of ore samples and 0.4 g of rock samples were digested (95 °C, 6 h) with 5 mL aqua regia ($HCl:HNO_3 = 3:1$, v/v). Certified reference material (NIST SRM 2711a, Montana soil) was digested using the same process. After storing overnight, the Hg concentrations in the digests were measured using cold vapor atomic absorption spectrometry (CVAAS), following the procedures detailed in Li et al. (2005). Recoveries of Hg for NIST SRM 2711a were between 90 and 110% ($n = 3$), and the relative variability of sample triplicates were < 8%.

The Hg isotope compositions of all samples were determined using Neptune Plus MC-ICP-MS (Thermo Electron Corp, Bremen, Germany) at the State Key Lab of Ore Deposit Geochemistry, Institute of Geochemistry, following the method by Yin et al. (2016). Mercury concentrations in sample digests were monitored by MC-ICP-MS using ^{202}Hg signals, and the Hg concentrations estimated by ^{202}Hg signals were within 10% of that measured by CVAAS. The ^{202}Hg intensities were about 1.3 V per ng/mL Hg and ^{202}Hg signals for blanks were about 1.0×10^{-3} V. Standard-sample bracketing (SSB) was used during the sample analysis. MDF is reported as ^{xxx}Hg, which means the per mil deviations from an international Hg standard, NIST SRM 3133 (Blum and Bergquist 2007):

$$\delta^{xxx}Hg = \left\{ \left[\left({}^{xxx}Hg/{}^{198}Hg \right)_{sample} / \left({}^{xxx}Hg/{}^{198}Hg \right)_{NIST3133} \right] - 1 \right\} \times 1000$$

where xxx is the mass of each Hg isotope ranging from 196 to 204. MIF of Hg isotopes is reported using $\Delta^{xxx}Hg$, which means the deviation of the measured isotope ratio from the theoretical ratio predicted by MDF and can be calculated using the following equations (Blum and Bergquist 2007):

$$\Delta^{199}Hg = \delta^{199}Hg - \left(\delta^{202}Hg \times 0.2520 \right)$$

$$\Delta^{200}Hg = \delta^{200}Hg - \left(\delta^{202}Hg \times 0.5024 \right)$$

$$\Delta^{201}Hg = \delta^{201}Hg - \left(\delta^{202}Hg \times 0.7520 \right)$$

The diluted solutions were prepared to have an acid concentration of 10–20%, and Hg concentrations and acid matrices of the NIST SRM 3133 were matched to the bracketed samples. UM-Almadén secondary standard solutions were diluted to 1 ng/mL Hg in 10% acid and measured in the same way as the samples. The overall mean and uncertainty for

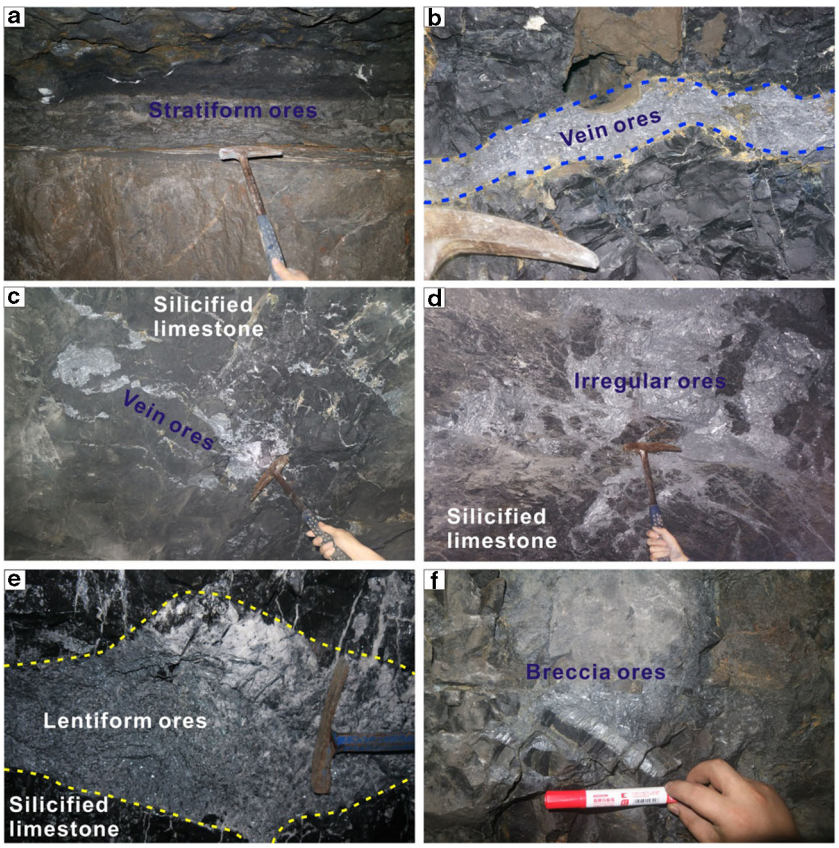

Fig. 3 Photographs of ore types. **a** Stratiform ores. **b**, **c** Vein ores. **d** Irregular ores. **e** Lentiform ores. **f** Breccia ores

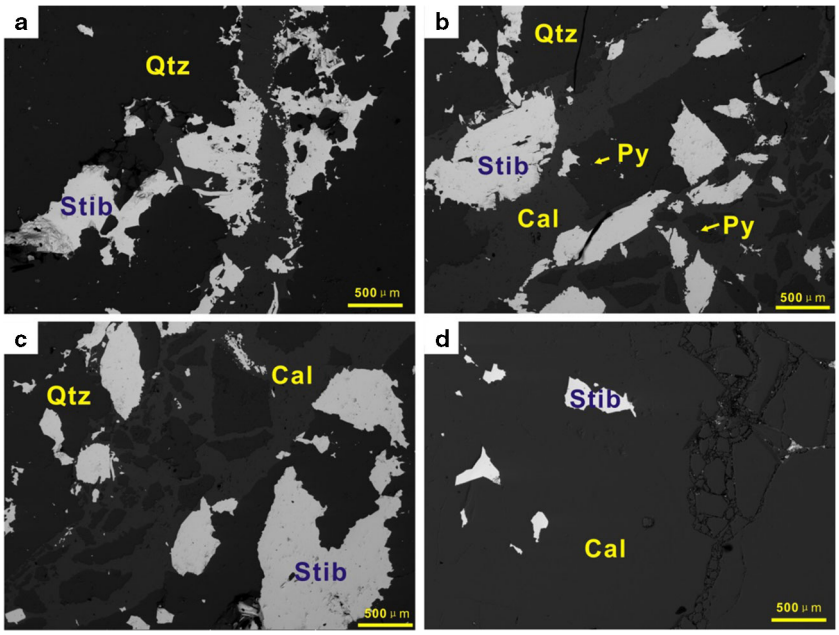

Fig. 4 Scanning electron microscopy images of ore types encountered at the Xikuangshan Sb deposit. **a** Quartz-stibnite ores. **b**, **c** Quartz-calcite-stibnite ores with minor pyrite. **d** Calcite-stibnite ore. Cal calcite, Py pyrite, Qtz quartz, Stib stibnite

UM-Almadén (δ^{202}Hg = − 0.55 ± 0.15‰; Δ^{201}Hg = − 0.04 ± 0.06‰; Δ^{199}Hg = − 0.01 ± 0.04‰, 2σ, n = 7) and NIST SRM 2711 (δ^{202}Hg: − 0.14 ± 0.09‰; Δ^{199}Hg: − 0.21 ± 0.04‰; Δ^{201}Hg: − 0.20 ± 0.05 ‰; 2σ, n = 3) are comparable with previous studies (Blum and Bergquist 2007; Sherman et al. 2009; Donovan et al. 2013; Yin et al. 2016).

In situ sulfur isotope analysis

In situ sulfur isotopic compositions of stibnites in ore samples and sedimentary pyrites in host rocks were analyzed by LA-MC-ICP-MS at the State Key Laboratory of Continental Dynamics, Northwest University, China. The laser ablation system (RESOlution M-50), consisted of an excimer laser (193 nm), a two-volume laser ablation cell (Laurin Technic S155, 155 mm × 105 mm), a squid smoothing device, and a computer-controlled high-precision X-Y stage, was linked to MC-ICP-MS (Nu Plasma 1700) for in situ S isotope analysis. The Nu 1700 MC-ICP-MS system equipped with sixteen Faraday cups and three ion counters was used to determine the sulfur isotopic compositions of the PSPTs. The cup configurations for sulfur were as follows: an H5 cup for ^{34}S, an Ax cup for ^{33}S, and an L4 cup for ^{32}S. Helium was used as carrier gas (0.28 L/min) for the laser ablation process, and it entered the cell body at its bottom to fill the cell. Helium from both bottom and top through the funnel cell entrained the sample aerosol and argon (0.98 L/min) was admixed downstream, in front of the squid signal smoothing device, into the MC-ICP-MS. Details on the method are given by Chen et al. (2017). Instrumental mass bias was corrected using the SSB approach with repeated measurements of the standard reference (IAEA-S-1, Ag_2S), before and after each sample. To monitor the accuracy of data during analysis, the in-house standard Cpy-1/GC (δ^{34}S = − 0.7 ± 0.3‰) was analyzed every 8 unknown spots. Analytical uncertainty of δ^{34}S is < 0.1‰.

Results

Mercury concentrations and isotopic compositions

The total Hg (HgT) concentrations and Hg isotopic compositions of the samples are summarized in Table 1. The Proterozoic basement metamorphic rocks and barren host rocks have low HgT concentrations of 0.02 to 0.06 ppm (mean = 0.04 ppm) and 0.44 to 1.25 ppm (mean = 0.77 ppm), respectively. In contrast, stibnite samples and altered host rocks showed high HgT concentrations, ranging from 11.25 to 97.43 ppm (mean = 37.51 ppm) and 3.85 to 8.09 ppm (mean = 6.21 ppm), respectively. The 15 stibnite samples show δ^{202}Hg ranging from 0.04 to 1.15‰ (mean = 0.41 ± 0.68‰, 2σ) and Δ^{199}Hg ranging from − 0.17 to − 0.03‰ (mean = − 0.11 ± 0.08‰, 2σ). The three altered rocks have δ^{202}Hg values of 0.07 to 0.52‰ (mean = 0.33 ± 0.30‰, 2σ) and Δ^{199}Hg of − 0.14 to − 0.02‰ (mean = − 0.04 ± 0.12‰, 2σ), which are similar to that of ore samples. The four barren rock samples show relatively lower δ^{202}Hg values (− 2.22 to − 0.04‰; mean = − 0.71 ± 2.04‰; 2σ) but similar Δ^{199}Hg (− 0.11 to 0.16‰; mean = − 0.01 ± 0.24‰, 2σ). The four metamorphic basement rocks have δ^{202}Hg values of − 0.36 to 0.60‰ (mean = 0.11 ± 1.04‰, 2σ) and Δ^{199}Hg of − 0.03 to 0.07‰ (mean = 0.00 ± 0.08‰, 2σ). The overall variations of Δ^{199}Hg for all samples (− 0.17 to − 0.02‰) are much higher than the analytical uncertainty for the UM-

Table 1 Mercury concentration and isotopic compositions in stibnite ores and potential source rocks for the Xikuangshan Sb deposit in central Hunan province

Sample types	Sample no.	Location and elevation of sample (m)	HgT (ppm)	δ^{202}Hg (‰)	δ^{201}Hg (‰)	δ^{200}Hg (‰)	δ^{199}Hg (‰)	Δ^{201}Hg (‰)	Δ^{200}Hg (‰)	Δ^{199}Hg (‰)
Stibnite ores	XKS-2@4	Level 2#; + 320	26.08	0.32	0.17	0.18	− 0.03	− 0.07	0.02	− 0.11
	XKS-3@3	Level 3#; + 300	59.71	0.04	− 0.12	− 0.05	− 0.09	− 0.15	− 0.07	− 0.10
	XKS-5@5	Level 5#; + 240	44.19	0.36	0.22	0.23	− 0.01	− 0.05	0.05	− 0.10
	XKS-7@1	Level 7#; + 190	80.24	0.10	− 0.06	0.03	− 0.13	− 0.13	− 0.02	− 0.16
	XKS-9-1	Level 9#; + 170	35.37	0.24	0.11	0.12	− 0.04	− 0.06	0.00	− 0.10
	XKS-11@3	Level 11#; + 136	25.35	0.05	− 0.02	0.02	− 0.09	− 0.06	− 0.01	− 0.10
	XKS13@8	Level 13#; + 78	14.19	0.39	0.26	0.27	0.00	− 0.03	0.07	− 0.10
	XKS-15@7	Level 15#; + 30	28.20	0.19	0.01	0.07	− 0.06	− 0.13	− 0.03	− 0.11
	XKS-19@1	Level 19#; − 34	16.61	0.56	0.35	0.24	0.04	− 0.07	− 0.04	− 0.10
	XKS-19@3	Level 19#; − 34	21.96	0.04	− 0.10	0.02	− 0.09	− 0.12	0.01	− 0.10
	XKS-23@3	Level 23#; − 120	35.60	1.04	0.62	0.53	0.16	− 0.16	0.00	− 0.10
	XKS-23@8	Level 23#; − 120	34.32	0.63	0.27	0.18	− 0.01	− 0.21	− 0.14	− 0.17
	XKS-25@1	Level 25#; − 142	11.25	0.58	0.32	0.30	0.02	− 0.11	0.02	− 0.12
	XKS-25@2	Level 25#; − 142	97.43	0.43	0.31	0.27	0.08	− 0.01	0.06	− 0.03
	XKS-25@3	Level 25#; − 142	32.17	1.15	0.78	0.57	0.13	− 0.09	− 0.01	− 0.16
Altered wall rocks	XKS-2@2	Level 2#; + 320	3.85	0.07	− 0.02	0.03	− 0.13	− 0.07	0.00	− 0.14
	XKS-7@6	Level 7#; + 190	8.09	0.41	0.23	0.18	0.00	− 0.08	− 0.03	− 0.10
	XKS-9@2	Level 9#; + 170	6.69	0.52	0.54	0.36	0.11	0.15	0.10	− 0.02
Barren wall rocks	XKS-2@1	Level 2#; + 320	0.78	− 0.04	− 0.07	− 0.02	− 0.12	− 0.04	0.00	− 0.11
	XKS-3@1	Level 3#; + 300	0.62	− 0.35	− 0.30	− 0.16	− 0.11	− 0.03	0.01	− 0.02
	XKS-4@2	Level 4#; + 300	1.25	− 0.21	− 0.18	− 0.10	− 0.14	− 0.02	0.00	− 0.09
	XKS-7@2	Level 7#; + 190	0.44	− 2.22	− 1.55	− 1.10	− 0.40	0.12	0.01	0.16
Basement metamorphic rocks	WXbd-2	Xuefengshan uplift belt	0.018	− 0.36	− 0.23	− 0.10	− 0.02	0.03	0.08	0.07
	WXbd-4		0.060	− 0.32	− 0.25	− 0.14	− 0.10	− 0.01	0.02	− 0.02
	WXbd-5		0.060	0.52	0.37	0.29	0.10	− 0.02	0.03	− 0.03
	WXbd-7		0.016	0.60	0.33	0.27	0.15	− 0.13	− 0.04	0.00

Almadén ($2\sigma = 0.04‰$). Most ore samples (11 of 15) with reliable MIF have $\Delta^{199}Hg/\Delta^{201}Hg$ ratios of 1.12 ± 0.38 (σ, $n = 11$), which approximate to the photo-reductive $\Delta^{199}Hg/\Delta^{201}Hg$ ratios of 1 to 1.3 (e.g., Bergquist and Blum 2007; Zheng and Hintelmann 2009). However, no discernable correlation trends were observed between HgT and either $\delta^{202}Hg$ or $\Delta^{199}Hg$.

Sulfur isotopic compositions

A total of 50 spots were analyzed, including 43 stibnite grains in ore samples and 7 pyrite grains in host rocks, and the results are shown in Table 2 and Fig. 5. The 43 stibnite grains show relatively narrow $\delta^{34}S$ ranges of + 6.8 to + 10.2‰, with an average of $+ 9.2 \pm 0.6‰$ ($n = 43$, 2σ). No systematic trends in $\delta^{34}S$ values are observed among all samples. In contrast, sedimentary pyrite grains from host rocks yield much higher $\delta^{34}S$ values of − 26.0 to + 21.9‰ ($+ 19.1 \pm 6.0‰$, 2σ, $n = 7$), suggesting they have a distinct origin from stibnite.

Discussion and conclusions

Hg isotope constraints on the sources of ore metals

In the Xikuangshan deposit, no Hg minerals were identified. It is believed that stibnite is the major carrier of Hg, not only as stibnite is the dominant sulfide mineral and the most Hg-enriched mineral (mean of HgT = 37.5 ppm) in this deposit but also due to that Hg can substitute with Sb in stibnite during its formation (Rytuba 2003). In fact, Sb and Hg are both chalcophile elements with similar chemical properties, suggesting that Hg generally has the same or similar sources as Sb (Arehart 1996; Hu et al. 2017; Nevolko et al. 2019).

The $\delta^{202}Hg$ values (0.04 to 1.15‰) and $\Delta^{199}Hg$ (− 0.17 to − 0.03 ‰) of stibnite, which present the isotopic signature of the majority of Hg in Xikuangshan, are within the range of reported in Hg and Pb-Zn deposits (Smith et al. 2005, 2008; Yin et al. 2016; Tang et al. 2017; Xu et al. 2018). Hg-MIF signals in natural samples were induced by Hg(II) photoreduction at Earth's surface (Blum et al. 2014; Yin et al. 2016). As hydrothermal processes do not induce Hg-MIF (Smith et al. 2005, 2008; Tang et al. 2017), Hg-MIF can be directly used as a source tracer of Hg in hydrothermal deposits. As shown in Fig. 6, significant Hg-MIF signals, with $\Delta^{199}Hg$ ranging from − 0.3 to 0.3‰, have been reported in sedimentary and metamorphic rocks, whereas magmatic rocks showed insignificant Hg-MIF ($\Delta^{199}Hg = 0 \pm 0.1‰$). Most of our stibnite samples showed significant Hg-MIF signals with $\Delta^{199}Hg$ of < − 0.1‰, which is distinct from that of magmatic rocks, suggesting either sedimentary rocks or metamorphic rocks contribute Hg in the Xikuangshan deposit. However, according to $\delta^{202}Hg$ values, our samples differ from sedimentary rocks but overlap with metamorphic rocks. As limited Hg-MDF ($\delta^{202}Hg < \pm 0.5‰$) occurs during the leaching of Hg from source rocks (Smith et al. 2008), the large difference of $\delta^{202}Hg$ between stibnite samples ($0.41 \pm 0.68‰$, 2σ, $n = 15$) and sedimentary rocks (− 3 to 1‰, with an average of − 0.73 $\pm 0.88‰$, 2σ, $n = 69$) suggests that Hg was not originated from sedimentary rocks. We, therefore, hypothesized that Hg, and

Table 2 In situ sulfur isotopic compositions of sulfide minerals in the Xikuangshan Sb deposit in central Hunan province

Analysis ID	Sample types	Minerals	$\delta^{34}S_{V\text{-}CDT}$ (‰)	2σ
XKS-s-1@01	Stibnite ores	Stibnite	9.93	0.15
XKS-s-1@02	Stibnite ores	Stibnite	9.85	0.13
XKS-1-2@01	Stibnite ores	Stibnite	10.16	0.13
XKS-1-2@02	Stibnite ores	Stibnite	9.89	0.12
XKS-1-8@01	Stibnite ores	Stibnite	9.81	0.14
XKS-1-15@01	Stibnite ores	Stibnite	9.84	0.13
XKS-2-2@01	Stibnite ores	Stibnite	6.81	0.13
XKS-2-2@02	Stibnite ores	Stibnite	9.00	0.14
XKS-3-5@01	Stibnite ores	Stibnite	9.89	0.12
XKS-3-7@01	Stibnite ores	Stibnite	7.56	0.12
XKS-3-7@02	Stibnite ores	Stibnite	7.83	0.11
XKS-4-1@01	Stibnite ores	Stibnite	9.43	0.13
XKS-4-3@01	Stibnite ores	Stibnite	9.59	0.12
XKS-4-3@02	Stibnite ores	Stibnite	9.23	0.12
XKS-5-5@01	Stibnite ores	Stibnite	7.34	0.13
XKS-5-5@02	Stibnite ores	Stibnite	8.31	0.13
XKS-6-3@01	Stibnite ores	Stibnite	9.78	0.13
XKS-6-3@02	Stibnite ores	Stibnite	9.72	0.12
XKS-6-3@03	Stibnite ores	Stibnite	9.63	0.12
XKS-6-3@04	Stibnite ores	Stibnite	9.48	0.12
XKS-6-3@05	Stibnite ores	Stibnite	9.95	0.12
XKS-7-9@01	Stibnite ores	Stibnite	10.23	0.12
XKS-7-9@02	Stibnite ores	Stibnite	9.91	0.12
XKS-7-9@03	Stibnite ores	Stibnite	9.89	0.11
XKS-9-5@01	Stibnite ores	Stibnite	10.05	0.12
XKS-9-5@02	Stibnite ores	Stibnite	10.10	0.12
XKS-11-3@01	Stibnite ores	Stibnite	7.91	0.11
XKS-11-3@02	Stibnite ores	Stibnite	8.06	0.13
XKS-13-6@01	Stibnite ores	Stibnite	7.81	0.13
XKS-13-6@02	Stibnite ores	Stibnite	8.13	0.14
XKS-13-8@01	Stibnite ores	Stibnite	9.91	0.13
XKS-13-8@02	Stibnite ores	Stibnite	10.12	0.13
XKS-15-1@01	Stibnite ores	Stibnite	7.99	0.12
XKS-15-1@02	Stibnite ores	Stibnite	7.49	0.13
XKS-19-2@01	Stibnite ores	Stibnite	8.36	0.12
XKS-19-2@02	Stibnite ores	Stibnite	7.64	0.20
XKS-23-8@01	Stibnite ores	Stibnite	9.64	0.11
XKS-23-8@02	Stibnite ores	Stibnite	9.77	0.12
XKS-23-8@03	Stibnite ores	Stibnite	9.95	0.13
XKS-23-8@04	Stibnite ores	Stibnite	9.99	0.12
XKS-25-2@01	Stibnite ores	Stibnite	9.12	0.12
XKS-25-2@02	Stibnite ores	Stibnite	9.84	0.12
XKS-25-2@03	Stibnite ores	Stibnite	9.44	0.12
XKS-1-8@01	Host rocks	Pyrite	18.74	0.17
XKS-1-8@02	Host rocks	Pyrite	21.94	0.31
XKS-1-10@01	Host rocks	Pyrite	21.43	0.12
XKS-1-10@02	Host rocks	Pyrite	18.52	0.13
XKS-1-12@01	Host rocks	Pyrite	19.90	0.46
XKS-1-12@02	Host rocks	Pyrite	17.75	0.38
XKS-13-6@01	Host rocks	Pyrite	− 25.97	0.56

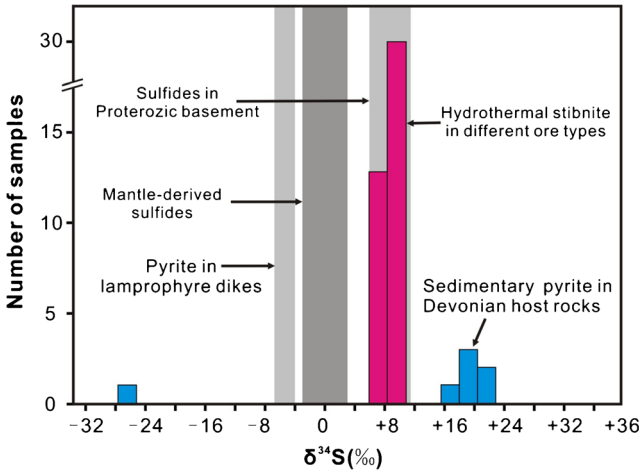

Fig. 5 Histogram of sulfur isotopic values of sulfide minerals from the Xikuangshan Sb deposit and potential source rocks. Data sources: mantle-derived sulfides: Chaussidon et al. (1989); pyrite in lamprophyre dikes: Yang (1986); sulfides in basement metamorphic rocks: Jiang (1990), Ma et al. (2003), and Gu et al. (2012)

Sb because of its similar chemical properties, were mainly derived from the Proterozoic basement metamorphic rocks. This is supported by the following additional evidence: (i) relatively "fresh" sedimentary rocks generally have very low Sb contents (average 0.9 ppm), whereas the Sb contents range up to 46 ppm in "altered" host rocks, indicating an external source of Sb (Ma et al. 2003; Hu et al. 2017); (ii) the Proterozoic basement metamorphic rocks have the highest Sb abundance (7.8 to 27.2 ppm; Lu et al. 2001; Ma et al. 2002) in the studied region; and (iii) leaching experiments demonstrated that the extractable Sb from basement rocks range between 20 and 90% at 200 °C (Ma et al. 2002),

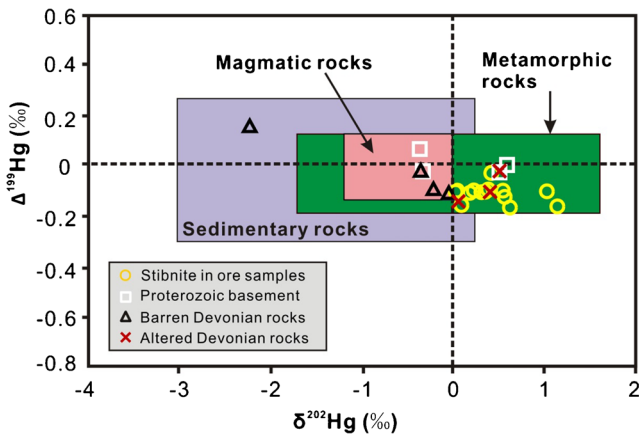

Fig. 6 Plot of δ^{202}Hg vs. Δ^{199}Hg values in stibnite from Xikuangshan Sb deposit, displaying a comparison of Hg isotopes between Xikuangshan deposit and lithological reservoirs. The range of sedimentary rocks was defined by the data from Smith et al. (2008), Thibodeau et al. (2016), Grasby et al. (2017), Gong et al. (2017), Yin et al. (2017), and Wang et al. (2018); the range of magmatic rocks was defined by the data from Smith et al. (2008) and metamorphic rocks are defined by the data from Smith et al. (2008) and Xu et al. (2018)

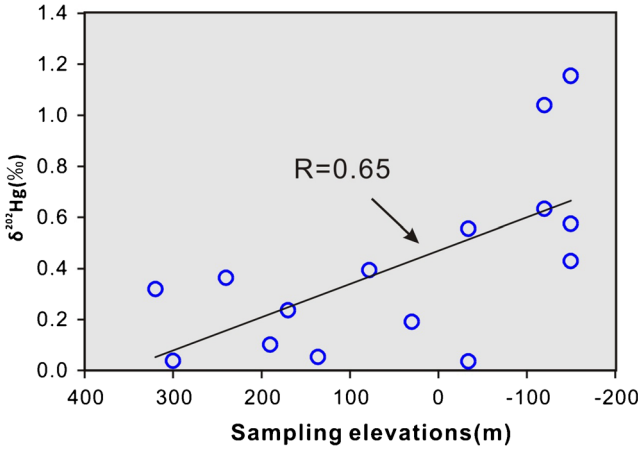

Fig. 7 Covariation of the sampling elevations vs. δ^{202}Hg in stibnite from the Xikuangshan Sb deposit

suggesting that they are likely significant metal contributors for this giant Sb deposit.

Although the leaching of Hg from source rocks does not induce a significant change of δ^{202}Hg (< ± 0.5‰; Smith et al. 2008), the stibnite samples show a variation of 1.11‰ in δ^{202}Hg, suggesting MDF may have occurred within the ore bodies. The boiling of hydrothermal fluids and redox reactions can result in significant Hg-MDF (up to 4‰ in δ^{202}Hg; Smith et al. 2005). Our results show a positive correlation between δ^{202}Hg and sampling depth (Fig. 7). A similar increase of δ^{202}Hg with depth has also been observed in epithermal systems in northern Nevada, USA, which has been explained by the evaporation of isotopically light Hg(0) during boiling of hydrothermal fluids (Smith et al. 2005). Boiling results in the loss of H_2S, CO_2, and Hg^0 from hydrothermal fluids, which cause the precipitation of sulfide minerals (Spycher and Reed 1989; Simmons and Christenson 1994; Christenson and Mroczek 2003). Laboratory experiments also confirmed that the volatilization of Hg^0 from aqueous phase cause Hg-MDF of > 1‰ in δ^{202}Hg, with the vaporized Hg^0 preferentially enriched in lighter Hg isotopes (Zheng et al. 2007). At Xikuangshan, recent fluid inclusion data provide some convincing evidence for the boiling process. For example, fluid inclusions with variable vapor/liquid proportions were observed within hydrothermal gangue minerals (Lin 2014). Additionally, dramatic fluctuations of pressures were recorded (Hu and Peng 2018) which could promote the occurrence of boiling during ore formation. Therefore, boiling is suggested as a major process responsible for the variation of δ^{202}Hg observed in this study.

Sources of sulfur in ore fluids

Stibnite is the principal sulfide in the ores of the Xikuangshan deposit, and in comparison with sulfide, the amount of sulfate minerals (barite and gypsum) is negligible; therefore, the δ^{34}S values of stibnite can represent that of the total sulfur in ore

fluids of this deposit (Seal 2006). Distinct from previous results using traditional methods ($\delta^{34}S$ values ranging from −3.3 to +16.8‰; Zou 1988; Ma et al. 2003; Fan et al. 2004; Yang et al. 2006a), our new results by in situ analysis suggest that the $\delta^{34}S$ values of stibnite ores, regardless of mineral paragenesis, are concentrated in a narrow range (+6.8 to +10.2‰; Fig. 5). The clustering of the sulfur isotope values indicates that the sulfur in ore fluids of different mineralization stages had a common origin or was derived from the same source region. As documented by Hu et al. (1996) and Peng et al. (2003), the NNE-striking 10-km-long lamprophyre dike is the only intrusion identified in the deposit area (Fig. 2a). Pyrite in this dike exhibits lighter $\delta^{34}S$ values (−6.3 to −3.9‰; Yang 1986), implying that the dominant sulfur in ore fluids was unlikely derived from the lamprophyric dike or the upper mantle. Additionally, a large variation of $\delta^{34}S$ values (−26.0 to +21.9‰) within pyrite grains within Devonian host rocks was observed (Table 2). If the ore fluids whose sulfur component was derived dominantly from the host rocks, the $\delta^{34}S$ values of ore fluids should be identical to that of Devonian initial seawater sulfate ($\delta^{34}S$ of +12.2 to +17.2‰; Ohmoto and Rye 1979). These $\delta^{34}S$ values, however, are much heavier than those of ore fluids obtained in this study (+6.8 to +10.2‰; mean = +9.2 ± 0.6‰), suggesting no significant contribution of sulfur from the Devonian host rocks.

Alternatively, our new in situ sulfur isotope data is comparable with the mean $\delta^{34}S$ values of sulfides in the Proterozoic basement rocks ($\delta^{34}S$ = +5.6 to +11.5‰; Jiang et al. 1990; Ma et al. 2003; Gu et al. 2012; Fig. 5). Therefore, we propose that the Proterozoic basement metamorphic rocks are likely the predominant source of sulfur during the formation of stibnites in the Xikuangshan deposit.

Implications for ore genesis

Available C-H-O isotopic data suggested that ore fluids for the Xikuangshan Sb deposit were dominated by deep-circulated meteoric water (Ma et al. 2003). Numerical modeling also suggested that the ore fluids mainly originated from meteoric water (Yang et al. 2006a). In addition, previous work noted that the Devonian host strata had low Sb content (0.7–2.3 ppm; Peng et al. 2001) making them an unlikely source of Sb. Using evidence from previous work in conjunction with Hg-S isotopes data obtained in this study, we propose that the Sb, Hg, and S transported by the ore fluids were predominantly derived from the underlying Proterozoic basement metamorphic rocks. A model can be invoked that assumes deep circulation of meteoric water, mobilization of Sb, Hg, and S from basement metamorphic rocks underlying the Xiangzhong basin, ascending of the hydrothermal fluids along deep faults, and subsequently deposition of Sb ore minerals within favorable structural traps resulting in the formation of the world-class Xikuangshan Sb deposit.

Acknowledgments We are grateful to Ryan Mathur and Stephen Kesler for their insightful and constructive comments. Bernd Lehmann and Thomas Monecke are thanked for careful editing of the manuscript and helpful comments.

Funding information This work was financially supported by projects of National Natural Science Foundation of China (41830432, 41703044, U1812402, and 41873047), the Strategic Priority Research Program (B) of Chinese Academy of Sciences (XDB18000000), West Light Foundation of the Chinese Academy of Sciences (Y7CR022000), and National Key R&D Program of China (2016YFC0600503). Shanling Fu is funded by the China Scholarship Council.

References

Arehart GB (1996) Characteristics and origin of sediment-hosted gold deposits: a review. Ore Geol Rev 11:383–403

Bergquist BA, Blum JD (2007) Mass-dependent and -independent fractionation of Hg isotopes by photoreduction in aquatic systems. Science 318:417–420

Bergquist BA, Blum JD (2009) The odds and evens of mercury isotopes: applications of mass-dependent and mass-independent isotope fractionation. Elements 5:353–357

BGMRHN (Bureau of Geology and Mineral Resource in Hunan Province) (1988) Regional geology of the Hunan province. Geological Publishing House, Beijing, pp 286–507 **(in Chinese with English summary)**

Blum JD, Bergquist BA (2007) Reporting of variations in the natural isotopic composition of mercury. Anal Bioanal Chem 388:353–359

Blum JD, Sherman LS, Johnson MW (2014) Mercury isotopes in earth and environmental sciences. Annu Rev Earth Planet Sci 42:249–269

Bühn B, Santos RV, Dardenne MA, de Oliveira CG (2012) Mass-dependent and mass-independent sulfur isotope fractionation ($\delta^{34}S$ and $\delta^{33}S$) from Brazilian Archean and Proterozoic sulfide deposits by laser ablation multi-collector ICP-MS. Chem Geol 312:163–176

Chaussidon M, Albarède F, Sheppard SMF (1989) Sulphur isotope variations in the mantle from ion microprobe analyses of micro-sulphide inclusions. Earth Planet Sci Lett 92:144–156

Chen XL, Jiang YH, Li SY, Liao ZH (1983) A preliminary study on the origin of the Xikuangshan antimony deposits in Hunan. Geological Review 5:486–493 **(in Chinese with English abstract)**

Chen YW, Bi XW, Fu SL, Dong SH (2016) Zircon U-Pb dating and Hf isotopes of the felsic dykes in the Longshan Au-Sb deposit in Central Hunan Province and their geological significance. Acta Petrol Sin 32:3469–3488 **(in Chinese with English abstract)**

Chen L, Chen KY, Bao ZA, Liang P, Sun TT, Yuan HL (2017) Preparation of standards for in situ sulfur isotope measurement in sulfides using femtosecond laser ablation MC-ICP -MS. J Anal At Spectrom 32:107–116

Christenson BW, Mroczek EK (2003) Potential reaction pathways of Hg in some New Zealand hydrothermal environments. In: Simmons SF, Graham I (eds) Volcanic, geothermal and ore-forming processes; rulers and witnesses of processes within the Earth, Society of Economic Geologists Special Publication, vol 10, pp 111–132

Craddock PR, Rouxel OJ, Ball LA, Bach W (2008) Sulfur isotope measurement of sulfate and sulfide by high-resolution MC-ICP-MS. Chem Geol 253:102–113

Darling JR, Storry CD, Hawkesworth CJ, Lightfoot PC (2012) In-situ Pb isotope analysis of Fe–Ni–Cu sulphides by laser ablation multi-collector ICPMS: new insights into ore formation in the Sudbury impact melt sheet. Geochim Cosmochim Acta 99:1–17

Dauphas N, van Zuilen M, Wadhwa M, Davis AM, Marty B, Janney PE (2004) Clues from Fe isotope variations on the origin of early Archean BIFs from Greenland. Science 306:2077–2080

Debret B, Beunon H, Mattielli N, Andreani M, Ribeiro da Costa I, Escartin J (2018) Ore component mobility, transport and mineralization at mid-oceanic ridges: a stable isotopes (Zn, Cu and Fe) study of the Rainbow massif (Mid-Atlantic Ridge 36°14' N). Earth Planet Sci Lett 503:170–180

Donovan PM, Blum JD, Yee D, Gehrke GE, Singer MB (2013) An isotopic record of mercury in San Francisco Bay sediment. Chem Geol 349-350:87–90

Fan DL, Zhang T, Ye J (2004) The Xikuangshan Sb deposit hosted by the Upper Devonian black shale series, Hunan, China. Ore Geol Rev 24: 121–133

Fu SL, Hu RZ, Bi XW, Chen YW, Yang JH, Huang Y (2015) Origin of Triassic granites in central Hunan Province, South China: constraints from zircon U-Pb ages and Hf and O isotopes. Int Geol Rev 57:97–111

Fu SL, Hu RZ, Batt GE, Danisik M, Evans NJ, Mi XF (2019) Zircon (U-Th)/He thermochronometric constraints on the mineralization of the giant Xikuangshan Sb deposit in central Hunan, South China. Mineral Deposita. https://doi.org/10.1007/s00126-019-00906-3

Gong Q, Wang XD, Zhao LS, Grasby SE, Chen ZQ, Zhang L, Li Y, Cao L, Li ZL (2017) Mercury spikes suggest volcanic driver of the Ordovician-Silurian mass extinction. Sci Rep 7:5304. https://doi.org/10.1038/s41598-017-05524-5

Grasby SE, Shen WJ, Yin RS, Gleason JD, Blum JD, Lepak RF, Hurley JP, Beauchamp B (2017) Isotopic signatures of mercury contamination in latest Permian oceans. Geology 45:55–58

Gu XX, Zhang YM, Schulz O, Vavtar F, Liu JM, Zheng MH, Zheng L (2012) The Woxi W–Sb–Au deposit in Hunan, South China: an example of Late Proterozoic sedimentary exhalative (SEDEX) mineralization. J Asian Earth Sci 57:54–75

Hou L, Peng HJ, Ding J, Zhang JR, Zhu SB, Wu SY, Wu Y, Ouyang HG (2016) Textures and in situ chemical and isotopic analyses of pyrite, Huijiabao Trend, Youjiang basin, China: implications for paragenesis and source of sulfur. Econ Geol 111:331–353

Hu AX, Peng JT (2018) Fluid inclusions and ore precipitation mechanism in the giant Xikuangshan mesothermal antimony deposit, South China: conventional and infrared microthermometric constraints. Ore Geol Rev 95:49–64

Hu RZ, Zhou MF (2012) Multiple Mesozoic mineralization events in South China-an introduction to the thematic issue. Mineral Deposita 47:579–588

Hu XW, Pei RF, Zhou S (1996) Sm-Nd dating for antimony mineralization in the Xikuangshan deposit, Hunan, China. Resour Geol 46: 227–231

Hu RZ, Fu SL, Huang Y, Zhou MF, Zhao CH, Wang YJ, Bi XW, Xiao JF (2017) The giant South China Mesozoic low-temperature metallogenic domain: reviews and a new geodynamic model. J Asian Earth Sci 137:9–34

Jiang ZY, Wei LM, Chen MY (1990) Sulfur isotopic study of sulfides from sedimentary strata and strata-bound deposits in Hunan. Guangdong and Guangxi of Southern China: Geochemica 19:117–126 **(In Chinese with English abstract)**

Jin JF, Tao Y, Zeng LJ (2001) The ore-forming fluid of Xikuangshan-type antimony deposits. Bull Mineral Petrol Geochem 3:156–164 **(in Chinese with English abstract)**

Kelley KD, Wilkinson JJ, Chapman JB (2009) Zinc isotopes in sphalerite from metal deposits in the red dog district, northern Alaska. Econ Geol 104:767–773

Kuang WL (2000) Research on the metallogenic model of Xikuangshan superlarge antimony deposit. World Geo 19:26–30 **(in Chinese with English abstract)**

Li ZH, Feng XB, He TR, Yan HY, Liang L (2005) Determination of total mercury in soil and sediment by aquaregia digestion in the water bath coupled with cold vapor atom fluorescence spectrometry. Bull Mineral Petrol Geochem 24:140–143 **(in Chinese with English abstract)**

Lin FM (2014) On the ore-forming fluid in the Xikuangshan antimony deposit, central Hunan. Center South University, Changsha, Master thesis, pp 1–62 **(in Chinese with English abstract)**

Liu GM, Jian HM (1983) Geological characteristics of the Xikuangshan antimony ore field. Mineral Deposits 2:43–49 **(in Chinese with English abstract)**

Liu HP, Zhang YL, Hu WQ (1985) A discussion on ore genesis of the Xikuangshan Sb deposit in Hunan. Hunan Geology 1:28–39 (n Chinese with English abstract)

Lu XW, Ma DS, Xie QL, Wang WY (2001) Trace element geochemical characteristics of Neoproterozoic-Paleozoic strata in western and central Hunan. Geology- Geochemistry 29:24–30 **(in Chinese with English abstract)**

Ma DS, Pan JY, Xie QL, He J (2002) Ore source of Sb (Au) deposits in Center Hunan: I. Evidences of trace elements and experimental geochemistry. Mineral Deposits 3:366–376 **(in Chinese with English abstract)**

Ma DS, Pan JY, Xie QL (2003) Ore sources of Sb (Au) deposits in Center Hunan: II. Evidence of isotopic geochemistry. Mineral Deposits 21: 78–87 **(in Chinese with English abstract)**

Mason PRD, Kosler J, de Hoog JCM, Sylvester PJ, Meffan-Main S (2006) In situ determination of sulfur isotopes in sulfur-rich materials by laser ablation multiple-collector inductively coupled plasma mass spectrometry (LA-MC-ICP-MS). J Anal At Spectrom 21:177–186

Mathur R, Marschik R, Ruiz J, Munizaga F, Leveille RA, Martin W (2002) Age of mineralization of the Candelaria Fe oxide Cu-Au deposit and the origin of the Chilean Iron Belt, based on Re-Os isotopes. Econ Geol 97:59–71

Mathur R, Brantley S, Anbar A, Munizaga F, Maksaev V, Newberry R, Vervoort J, Hart G (2010) Variation of Mo isotopes from molybdenite in high-temperature hydrothermal ore deposits. Mineral Deposita 45:43–50

Meng YM, Qi HW, Hu RZ (2015) Determination of germanium isotopic compositions of sulfides by hydride generation MC-ICP-MS and its application to the Pb–Zn deposits in SW China. Ore Geol Rev 65: 1095–1109

Morelli R, Creaser RA, Stuart FM, Selby D, Graupner T (2007) Age and source constraints for the giant Muruntau gold deposit, Uzbekistan, from coupled Re-Os-He isotopes in arsenopyrite. Geology 35:795–798

Nevolko PA, Hnylko OM, Mokrushnikov VP, Gibsher AS, Redin YO, Zhimulev FI, Drovzhak AE, Svetlitskaya TV, Fomynikh PA, Karavashkin MI (2019) Geology and geochemistry of the Kadamzhai and Chauvai gold-antimony-mercury deposits: implications for new province of Carlin-type gold deposits at the Southern Tien Shan (Kyrgyzstan). Ore Geol Rev 105:551–571

Ohmoto H, Rye RO (1979) Isotopes of sulfur and carbon. In: Barnes HL (ed) Geochemistry of hydrothermal ore deposits, 2nd edn. Wiley, New York, pp 509–567

Peng JT, Hu RZ, Deng HL, Su WC (2001) Strontium isotope geochemistry of Xikuangshan antimony deposit, center Hunan. Geochemica 3:248–256 **(in Chinese with English abstract)**

Peng JT, Hu RZ, Burnard PG (2003) Samarium-neodymium isotope systematics of hydrothermal calcite from the Xikuangshan antimony deposit (Hunan, China): the potential of calcite as a geochronometer. Chem Geol 200:129–136

Rytuba JJ (2003) Mercury from mineral deposits and potential environmental impact. Environ Geol 43:326–338

Schwartz MO (1997) Mercury in zinc deposits: economic geology of a polluting element. Int Geol Rev 39:905–923

Seal RR (2006) Sulfur isotope geochemistry of sulfide minerals. Rev Mineral Geochem 61:633–677

Sherman LS, Blum JD, Nordstrom DK, McCleskey RB, Barkay T, Vetriani C (2009) Mercury isotopic composition of hydrothermal systems in the Yellowstone Plateau volcanic field and Guaymas Basin sea-floor rift. Earth Planet Sci Lett 279:86–96

Shi MK, Fu BQ, Jin XX (1993) Antimony metallogeny in central part of Hunan province. Hunan Press of Science and Technology, Changsha, pp 1–151 **(in Chinese)**

Simmons SF, Christenson BW (1994) Origins of calcite in a boiling geothermal system. Am J Sci 294:361–400

Smith CN, Kesler SE, Klaue B, Blum JD (2005) Mercury isotope fractionation in fossil hydrothermal systems. Geology 33:825–828

Smith CN, Kesler SE, Blum JD, Rytuba JJ (2008) Isotope geochemistry of mercury in source rocks, mineral deposits and spring deposits of the California Coast Ranges, USA. Earth Planet Sci Lett 269:399–407

Sonke JE, Schofer J, Chmeleff J, Audry S, Blanc G, Dupre B (2010) Sedimentary mercury stable isotope records of atmospheric and riverine pollution from two major European heavy metal refineries. Chem Geol 279:90–100

Spycher N, Reed MH (1989) Evolution of a Broadlands-type epithermal fluid along alternative P-T path: implications for the transport and deposition of base, precious and volatile metals. Econ Geol 84:328–359

Tang YY, Bi XW, Yin RS, Feng XB, Hu RZ (2017) Concentrations and isotopic variability of mercury in sulfide minerals from the Jinding Zn-Pb deposit, Southwest China. Ore Geol Rev 90:958–969

Tao Y, Gao ZM, Jin JF, Zeng LJ (2002) Ore-forming conditions of Xikuangshan-type antimony deposits in central Hunan. Earth Sci 2:184–195 **(in Chinese with English abstract)**

Thibodeau AM, Ritterbush K, Yager JA, West AJ, Ibarra Y, Bottjer DJ, BerelsonWM BBA, Corsetti FA (2016) Mercury anomalies and the timing of biotic recovery following the end-Triassic mass extinction. Nat Commun 7:1–8

Wang XD, Cawood PA, Zhao H, Zhao LS, Grasby SE, Chen ZQ, Wignall PB, Lv ZY, Han C (2018) Mercury anomalies across the end Permian mass extinction in South China from shallow and deep water depositional environments. Earth Planet Sci Lett 496:159–167

Xie GQ, Peng JT, Hu RZ, Jia DC (2001) Geological characteristics of lamprophyres in the Xikuangshan antimony ore deposits, Hunan province. Acta Petrol Sin 17:629–636 **(in Chinese with English abstract)**

Xie GQ, Mao JW, Li W, Fu B, Zhang ZY (2019) Granite-related Yangjiashan tungsten deposit, southern China. Mineral Deposita 54:67–80

Xu CX, Yin RS, Peng JT, Hurley JP, Lepak RF, Gao JF, Feng XB, Hu RZ, Bi XW (2018) Mercury isotope constraints on the source for sediment-hosted lead-zinc deposits in the Changdu area, southwestern China. Mineral Deposita 53:339–352

Yang SQ (1986) On inquiry about the genesis of Hunan antimony deposit and prospecting direction. Hunan Geology 4:12–25 **(in Chinese with English abstract)**

Yang RY, Ma DS, Bao ZY, Pan JY, Cao SL, Xia F (2006a) Geothermal and fluid flowing simulation of ore-forming antimony deposits in Xikuangshan. Science in China Series D: Earth Science 8:862–871

Yang DS, Shimizu M, Shimazaki H, Li XH, Xie QL (2006b) Sulfur isotope geochemistry of the supergiant Xikuangshan Sb deposit, central Hunan, China: constraints on sources of ore constituents. Resour Geol 56:385–396

Yao JL, Shu LS, Cawood PA, Li JY (2016) Delineating and characterizing the boundary of the Cathaysia Block and the Jiangnan orogenic belt in South China. Precambrian Res 275:265–277

Yin R, Feng X, Shi W (2010) Application of the stable-isotope system to the study of sources and fate of Hg in the environment: a review. Appl Geochem 25:1467–1477

Yin RS, Feng XB, Hurley JP, Krabbenhoft DP, Lepak RF, Hu RZ, Zhang Q, Li Z, Bi XW (2016) Mercury isotopes as proxies to identify sources and environmental impacts of mercury in sphalerites. Sci Rep 6:1–8

Yin RS, Xu LG, Lehmann B, Lepak RF, Hurley JP, Mao JW, Feng XB, Hu RZ (2017) Anomalous mercury enrichment in Early Cambrian black shales of South China: mercury isotopes indicate a seawater source. Chem Geol 467:159–167

Yin RS, Deng CZ, Lehmann B, Sun GY, Lepak RF, Hurley JP, Zhao CH, Xu GW, Tan QP, Xie GZ, Hu RZ (2019) Magmatic-hydrothermal origin of mercury in Carlin-style and epithermal gold deposits in China: evidence from mercury stable isotopes. ACS Earth and Space Chemistry 3:1631–1369

Yuan HL, Liu X, Chen L, Bao ZA, Chen KY, Zong CL, Li XC, Qiu JWH (2018) Simultaneous measurement of sulfur and lead isotopes in sulfides using nanosecond laser ablation coupled with two multi-collector inductively coupled plasma mass spectrometers. J Asian Earth Sci 154:386–396

Zhao JH, Zhou MF, Yan DP, Zheng JP, Li JW (2011) Reappraisal of the ages of Neoproterozoic strata in South China: no connection with the Grenvillian orogeny. Geology 39:299–302

Zheng W, Hintelmann H (2009) Mercury isotope fractionation during photoreduction in natural water is controlled by its Hg/DOC ratio. Geochim Cosmochim Acta 73:6704–6715

Zheng W, Foucher D, Hintelmann H (2007) Mercury isotope fractionation during volatilization of Hg (0) from solution into the gas phase. J Anal At Spectrom 22:1097–1104

Zhu CW, Wen HJ, Zhang YX, Fu SH, Fan HF, Cloquet C (2017) Cadmium isotope fractionation in the Fule Mississippi Valley-type deposit, Southwest China. Mineral Deposita 52:675–686

Zou TX (1988) Geochemica characteristics and ore-forming mechanism of the antimony ore field of Xikuangshan, Hunan. Journal of Guilin College of Geology 8:187–195 **(in Chinese with English abstract)**